PAPER

Infrared sensitive mixed phase of V_7O_{16} and V_2O_5 thin-films†

Anchal Rana,[a] Aditya Yadav,[b] Govind Gupta [ID][b] and Abhimanyu Rana [ID] *[a]

We report an infrared (IR) sensitive mixed phase of V_7O_{16} and V_2O_5 thin films, grown by cathodic vacuum arc-deposition on glass substrates at relatively low temperatures. We have found that the mixed phase of V_7O_{16} and V_2O_5 can be stabilized by post-annealing of amorphous V_xO_y between 300–400 °C, which gets fully converted into V_2O_5 after annealing at higher temperatures ~450 °C. The local conversion from V_xO_y to V_2O_5 has also been demonstrated by applying different laser powers in Raman spectroscopy measurements. The optical transmission of these films increases as the content of V_2O_5 increases but the electrical conductivity and the optical bandgap decrease. These results are explained by the role of defects (oxygen vacancies) through the photoluminescence (PL) and time-resolved photoluminescence (TRPL) measurements. The IR sensitivity of the mixed phase is explained by the plasmonic absorption by the V_7O_{16} degenerate semiconductor.

Introduction

Infrared (IR) sensitive materials have been of significant interest for IR sensors and smart windows in which the resistance or the optical transmission can be modulated by heating or IR radiation.[1,2] Therefore, many low-bandgap semiconductors,[3,4] quantum-well heterostructures[5] and high-temperature-superconductors[6,7] are intensively studied. However, these materials need to be cooled at lower temperatures for these applications. Vanadium-based oxides, found in more than 52 stable and metastable phases, have been investigated for developing uncooled devices as they show metal–insulator transitions (MIT) close to room temperatures under different external stimuli such as thermal, electrical, and optical.[8–14] Vanadium (V) can have oxidation states varying from +2 to +5, where V_2O_3, VO_2, and V_2O_5 are the most studied phases but other non-stoichiometric phases such as V_3O_7, V_4O_9, V_6O_{13}, V_7O_{16} have also been reported, that occur due to the presence of more than one valency of V atom in a single crystal structure.[14–17] Although, VO_2 (having V^{4+} valency) has been the most preferred phase for IR sensors[10,11,18] and smart windows due to sharp MIT close to room temperature,[19–22] it has limitations of growing in the right phase on arbitrary substrates at low temperatures. On the other hand, V_2O_5 having a layered structure is important for energy storage electrodes,[23–26] gas sensors[27–29] and chromogenic applications.[30–32] However, the

applicability of the pure V_2O_5 phase is again largely restricted due to high temperature growth and poor electrical conductivity. The mixed phase of VO_2 and V_2O_5 has been reported to give enhanced IR sensitivity.[33] Other phases such as V_7O_{16} could be promising for these applications which has the mixture of both V^{4+} and V^{5+} arranged in a layered crystal structure.[15,34,35] However, there are very few reports on V_7O_{16} phase which has been reported during chemical synthesis of V_2O_5 nanotubes[28,35] or in thin film form when grown under oxygen deficient conditions using pulsed laser deposition[29] and atomic layer deposition.[15] There is a clear research gap for in-depth understanding of electronic and optical properties of V_7O_{16} for any practical application in smart windows and IR sensors. Here, we systematically tune the contents of V_7O_{16} and V_2O_5 in a mixed phase (also changing the V^{4+} and V^{5+} ratio) by post-annealing of amorphous vanadium oxide thin films grown by cathodic vacuum arc-deposition. We report a strong modulation of electrical resistance and optical transmission in these films with IR radiation and temperature.

Materials and methods

First an amorphous vanadium oxide thin films were grown on high-grade barium-borosilicate 7059 glass substrates using cathodic vacuum arc-deposition by evaporating a vanadium metal target (~99.99% purity) in the presence of oxygen at a partial pressure of $\sim 1 \times 10^{-3}$ mbar, arc current of ~150 A, substrate temperature ~200 °C and substrate bias of −60 V. These films were then taken out and annealed in air at different temperatures *i.e.*, ~300 °C, ~350 °C, ~400 °C, ~450 °C, and 520 °C for 2 hours. The unannealed sample will be called as $S_{as-grown}$ and other annealed sampled as S_{300}, S_{350}, S_{400}, S_{450}, and

[a]*Centre for Advanced Materials and Devices, School of Engineering and Technology, BML Munjal University, Sidhrawali, Gurugram-122413, Haryana, India. E-mail: rana.abhimanyu@gmail.com*

[b]*CSIR-National Physical Laboratory, K. S. Krishnan Marg, New Delhi, 110012, India*
† Electronic supplementary information (ESI) available. See DOI: https://doi.org/10.1039/d3ra00752a

S_{520} in this manuscript. The Raman spectroscopy was carried out using a commercial spectrometer by WiTech (Alpha 300) having a green laser of 532 nm wavelength. The crystal structure was confirmed by X-ray diffraction (XRD, Panalytical Empyrean Model) by scanning 2θ ranging from 10° to 90° at a step size of 0.02° using Cu Kα radiation ($\lambda \sim 1.54$ Å). The X-ray photoelectron spectroscopy (XPS) was carried out using XPS/ESCA, K-ALPHA+, Thermo Fisher Scientific. The deconvolution and fitting of XPS data of was performed using XPSpeak41 software. The optical transmission spectra were obtained in the wavelength range from 380 nm to 800 nm using a UV-visible spectrometer by PerkinElmer LAMBDA 365 model. Electrical measurements were performed using a four-probe setup equipped with Keithley electrometers. The IR sensing measurements were carried out using the IR source by Newport model 6363IR having intensity $\sim$438 W m^{-2}. Photoluminescence (PL) and time-resolved photoluminescence (TRPL) were recorded at the excitation wavelength of $\sim$350 nm and $\sim$266 nm (pulsed) using Edinburgh (FLS 980D2D2) set-up.

Results and discussion

The XRD patterns of $S_{as-grown}$, S_{300}, S_{350}, S_{400}, S_{450}, and S_{520} are shown in Fig. 1(a) with their corresponding photographs in the inset. Apparently, the photographic images show a clear change in colour from black (of amorphous films) to the yellowish orange after annealing. There is also a clear transition in XRD spectra from a broad hump in $S_{as-grown}$ to sharp peaks in annealed samples at $\sim$15.3°, $\sim$20.18°, $\sim$21.65°, $\sim$31.04°, $\sim$41.21° and $\sim$41.87° related to (020), (001), (011), (040), (002), and (012) crystalline planes of the pure orthorhombic phase of V_2O_5 respectively. However, the peak at $\sim$24.5° confirms the

presence of the V_7O_{16} triclinic phase[15,34] in S_{350} and S_{400} samples.

To further confirm the presence of V_7O_{16}, the X-ray photoelectron spectroscopy (XPS) were performed on S_{300} and S_{520}, as shown in Fig. 1(b, c) and (d, e) respectively. The binding energy peak $\sim$284.8 eV of carbon 1s orbital was used to compensate the shifts in other peaks due to charging. The XPS spectra for 2p orbitals of vanadium (V) has two peaks corresponding to $2p_{3/2}$ and $2p_{1/2}$ due to the spin–orbit splitting of $\sim$7.5 eV. However, each peak $2p_{3/2}$ and $2p_{1/2}$ were further deconvoluted that correspond to the presence of V^{4+} ($\sim$516.5 eV & $\sim$524 eV) and V^{5+} ($\sim$517.5 eV & $\sim$525 eV).[15,36] The peak at $\sim$530 eV is related to 1s oxygen in vanadium oxygen bonds,[37,38] but other peaks at higher energies $\sim$532 eV are due to free hydroxyl groups adsorbed on the hydrophilic surfaces.[39] The ratio of V^{4+} and V^{5+} contents in S_{300} and S_{520}, estimated by the dividing the area under the curve of respective peaks, is found to be consistent with literature,[15,40] implying higher V^{4+} content in these samples having V_7O_{16} phase. In S_{520}, peaks corresponding to V^{4+} were observed because of the photoreduction of V^{5+} in V_2O_5 phase.[41]

The Raman spectroscopic results of these films are compared in Fig. 2. Due to the amorphous nature of $S_{as-grown}$ film, no sharp peaks were observed but as annealing temperature exceeds 300 °C, sharp peaks start appearing. The Raman spectra for S_{450} and S_{520} shows peaks at $\sim$101, $\sim$144, $\sim$194, $\sim$282, $\sim$304, $\sim$404, $\sim$483, $\sim$507, $\sim$528, $\sim$699, and $\sim$992 cm^{-1} due to different vibrational modes of V_2O_5 phase,[14,15,42–44] as description given in Table 1. Especially, the strongest peak at $\sim$144 cm^{-1} arises from the V–O–V chains of the layered structure of α-V_2O_5, as shown in Fig. 2(b). For the samples annealed below 400 °C (S_{300} and S_{350}), the peaks around $\sim$158, $\sim$255, $\sim$294, $\sim$832, $\sim$870, $\sim$970 cm^{-1} confirms the presence of V_7O_{16}
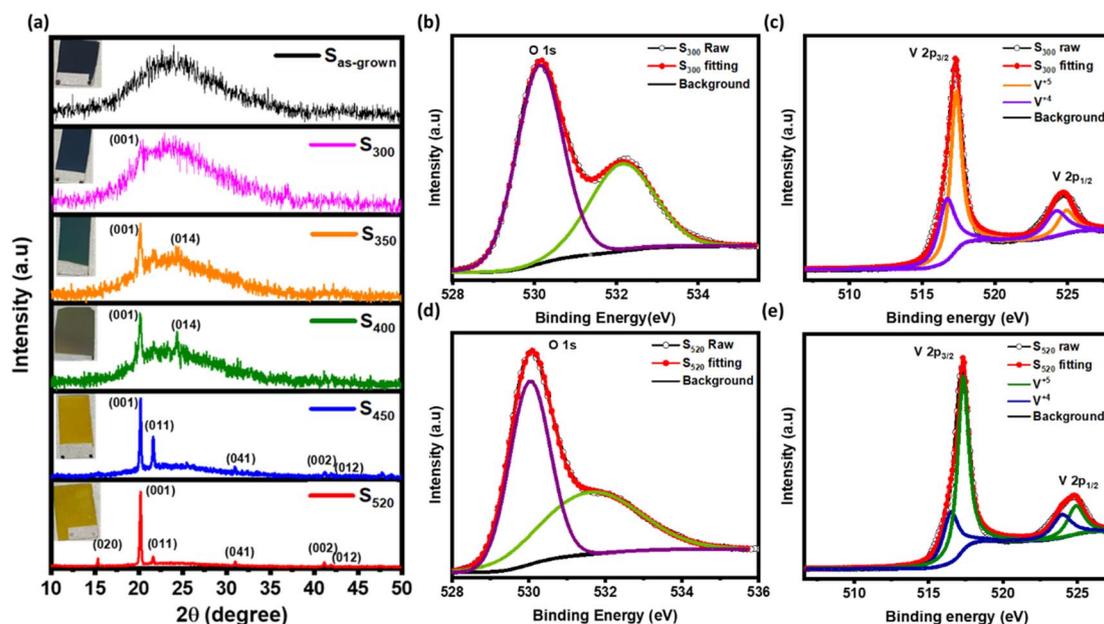

Fig. 1 (a) X-ray diffraction (XRD) spectra of vanadium oxide thin films annealed at various temperature. X-ray photoelectron spectroscopy (XPS) spectra of (b and c) S_{300} and (d and e) S_{520} samples shows V(2p) and O(1s) peaks.
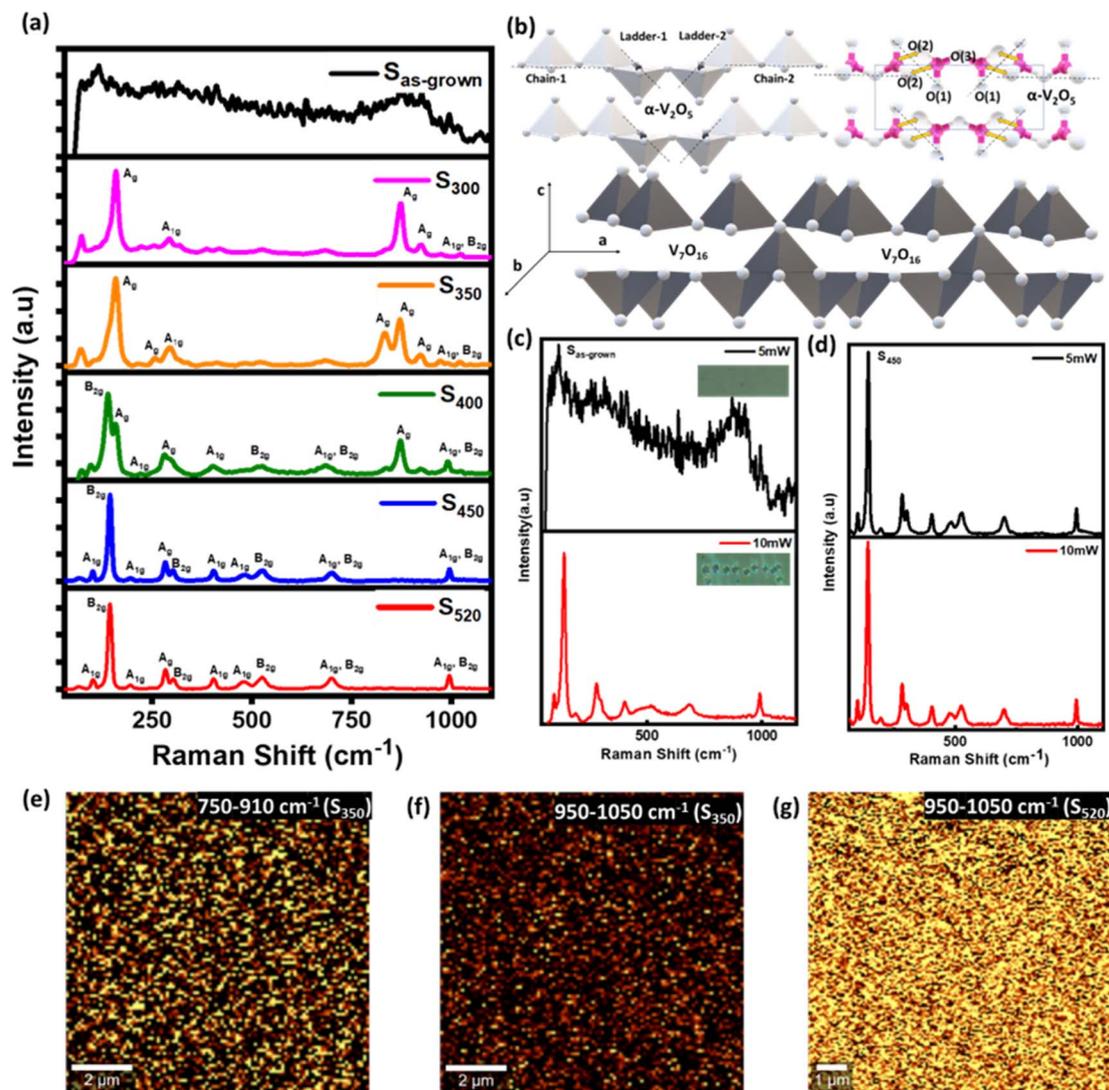
Fig. 2 (a) Raman spectra of vanadium oxide thin films annealed at various temperatures; (b) the crystal structure of α-V$_2$O$_5$ and V$_7$O$_{16}$; (c and d) S$_{as-grown}$ and S$_{450}$ samples at the laser power 5 mW and 10 mW laser power; (e–g) Raman mapping of the S$_{350}$ and S$_{520}$ samples.

phase, also consistent with the earlier studies.[14,44,45] It is to be noted that the presence of other polymorphs of V$_2$O$_5$ (β- γ-)[14,26,42,44] cannot be completely ruled out using Raman spectroscopy due to overlapping peak positions.[14] Fig. 2(b) shows the schematic of V$_7$O$_{16}$ phase where the layered structure resembles to α-V$_2$O$_5$, causing the peak ∼144 cm^{-1} to be shifted to higher wavenumber ∼158 cm^{-1}. However, the other vibrational modes related to ladder steps (LS) seems to be missing in V$_7$O$_{16}$, indicating the absence of LS in this phase. Clearly, other peaks at ∼255, ∼294, ∼832, ∼870, and ∼970 cm^{-1} could be assigned to the vibrational modes of V=O bonds (A$_g$ symmetry).[15] Also, the Raman spectroscopy performed at different laser powers (5 mW to 10 mW) in Fig. 2(c) and (d) shows the immediate conversion of amorphous phase to V$_2$O$_5$, unlike the annealed samples. Similar conversion was also observed by other groups in case of chemically synthesized VO$_x$ nanotubes.[43] This study opens further questions of stabilizing the intermediate phase of V$_7$O$_{16}$ using laser heating and open the opportunities for applications in laser writing for high

security tags and detection Fig. 2(e)–(g) shows the Raman mapping of S$_{350}$ and S$_{520}$ samples. Since the Raman spectra of the S$_{350}$ show the characteristic peaks at ∼832 cm^{-1}, 870 cm^{-1}, 920 cm^{-1} and S$_{520}$ at 994 cm^{-1}, we performed Raman mapping by selecting two wavelengths range from 750–910 cm^{-1} and 950–1050 cm^{-1} so that we could capture the regions of V$_7$O$_{16}$ and V$_2$O$_5$ spatially in 10 × 10 μm^2 area. In Fig. 2(e) and (f), for S$_{350}$ both V$_7$O$_{16}$ and V$_2$O$_5$ phases can be seen. On the other hand, for S$_{520}$ the brighter region mostly cover the V$_2$O$_5$ with some minor black regions due to some other phases.

Fig. 3(a) shows the optical transmission spectra of S$_{as-grown}$, S$_{300}$, S$_{350}$, S$_{400}$, S$_{450}$, and S$_{520}$. Apparently, the transmittance gradually increases with increasing the annealing temperature, and the maximum transmittance was observed in sample S$_{400}$. The optical band gap was calculated for all the samples by using Tauc's equations.[46] The calculated energy band gap of these samples decreases from ∼2.85 eV to 2.2 eV for the samples annealed at higher temperatures [Fig. 3(c)].

Table 1 Raman-active phonon modes in mixed phase of V_7O_{16} and V_2O_5 thin-films

ν (cm^{-1})	Description	Phonon modes
101	In phase rotation of the V_2O_4 ladder step (LS) unit in b-axis (crystalline V_2O_5)[14,42]	A_{1g}
144	Skeleton bending of V–O–V chain (crystalline V_2O_5)[14]	B_{2g}
158	Skeleton bending of V–O–V chain (crystalline V_7O_{16})[14,15]	A_g
194	Bending of O(2)–V–O(3) (crystalline V_2O_5)[14]	A_{1g}
255	Vibration of the V=O bond (crystalline V_7O_{16})	A_g
282	Bending of V=O (crystalline V_2O_5)[14]	A_{1g}
294	Bending of V=O (crystalline V_7O_{16})	A_g
304	Bending of V–O(2) (crystalline V_2O_5)[14]	B_{2g}
404	Angle-bending of V–O(3)–V bonds (crystalline V_2O_5)[14]	A_{1g}
483	Symmetric stretching of V–O(3)–V bonds (crystalline V_2O_5)[14]	A_{1g}
507	Stretching vibrations of V–O(2) bonds (crystalline V_2O_5)[14]	B_{2g}
528	Stretching vibrations of V–O(2) bonds (crystalline V_2O_5)[14]	A_{1g}
699	Asymmetric stretching of V–O(2)–V bridge (crystalline V_2O_5)	A_{1g}, B_{2g}
832	Stretching vibration of the V=O bond (crystalline V_7O_{16})[14,15]	A_g
870	Stretching vibration of the V=O bond (crystalline V_7O_{16})[14,15]	A_g
920	Stretching vibrations of V^{4+}=O bond (due to oxygen vacancies)[15]	A_g
992	Stretching vibration of V=O (crystalline V_2O_5)[14]	A_{1g}, B_{2g}

Usually, the amorphous semiconductors exhibit band-tailing due to the structural disorder which can be quantified as Urbach energy (E_u) shown in Fig. 3(b). The amorphous $S_{as-grown}$ sample clearly having more defects shows highest E_u value which decreases by increasing annealing temperature, that indicate the defects are significantly reduced after annealing. The electrical conductivity (measured by four-probe) also decreases for the samples annealed at higher temperatures, as shown in Fig. 3(d). Fig. 3(c) and (d) also shows the optical transmission integrated over the wavelength from 400–800 nm plotted on right Y-axis, having clear correlation with the electronic properties. The results are explained by considering a band-model shown in Fig. 3(e). Although the band gap of V_7O_{16} is higher than the V_2O_5, it still has high conductivity due to the presence of more V^{4+} content, that contribute extra electrons in 3d conduction band. Also, the amorphous and low-temperature annealed samples are expected to have large number of defects and oxygen vacancies, that can even push the Fermi level into the conduction band, making V_7O_{16} a degenerate semiconductor.[23] Therefore, the overall conductivity of mixed phase is higher than the V_2O_5 due to the presence of V_7O_{16}. On the other hand, the samples annealed at high-temperature are defects free, despite having a lower bandgap and the Fermi level lies in the band gap. The dynamic resistance
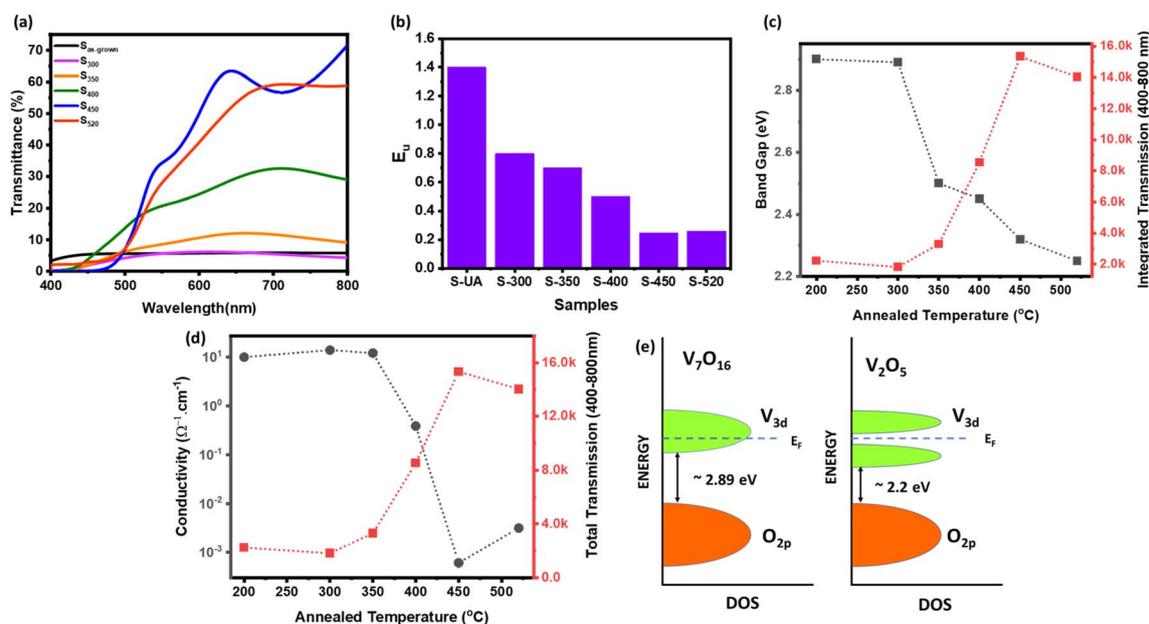

Fig. 3 (a) Optical transmission of vanadium oxide thin films annealed at different temperatures (b) Urbach energy of the samples (c) correlated with bandgaps and (d) conductivity of thin films (e) schematic band diagram of V_2O_5 and V_7O_{16}.
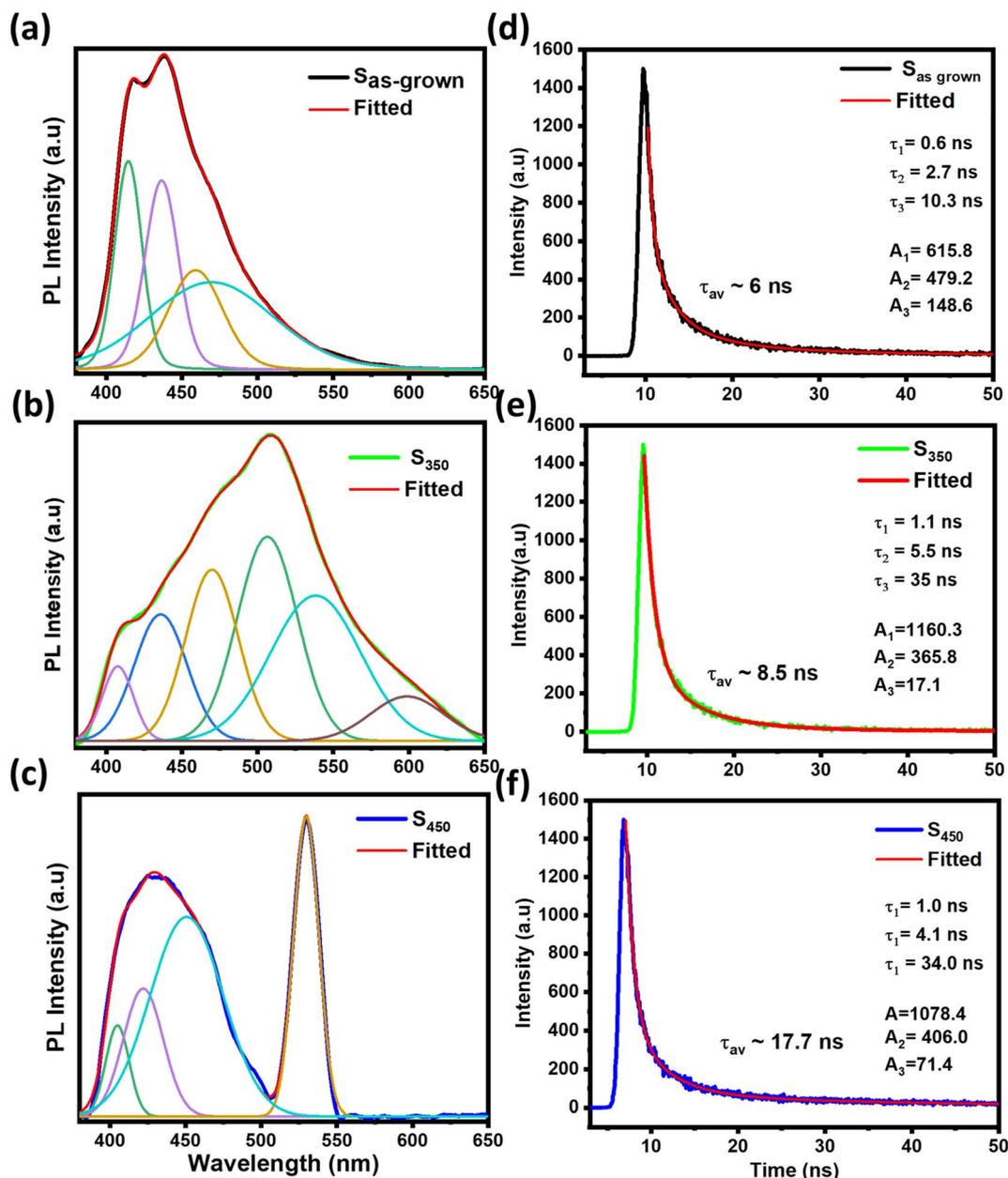
Fig. 4 (a–c) The photoluminescence (PL) and (d–f) time-resolved photoluminescence (TRPL) spectra of $S_{as-grown}$, S_{350} and S_{450} samples.

versus temperature measurements also confirms the metallic behavior of mixed phase, where the resistance is found to increase with temperature compared to pure V_2O_5 showing a typical decrease in resistance with temperature of semi-conducting behavior, as shown in ESI Fig. S1.† The correlation of transmission with conductivity in Fig. 3(c) and (d) can be explained by reflection and absorption caused by higher metallicity and defect states, respectively.

The photoluminescence (PL) and time-resolved-photoluminescence (TRPL) results of $S_{as-grown}$, S_{350}, and S_{450} are shown in Fig. 4. The peaks in PL spectra were deconvoluted using Gaussian function. The highest intensity peaks at ~438 nm, ~507 nm, ~530 nm can be assigned to the band-edge

transitions from V_{3d} conduction band to O_{2p} valence band,[37] matching the bandgap value of each sample measured by UV-vis measurement in Fig. 3. The peaks at longer wavelengths in NIR can be assigned to the electronic transitions in mid-gap states

Table 2 Time-resolved photoluminescence (TRPL) parameters for the $S_{as-grown}$, S_{350} and S_{450} samples

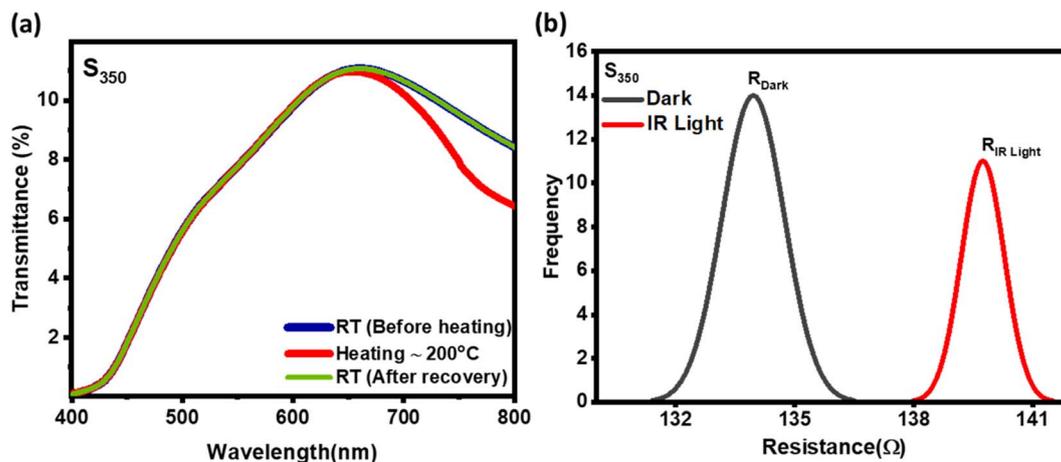| Sample	A_1	A_2	A_3	τ_1 (ns)	τ_2 (ns)	τ_3 (ns)	$\tau_{average}$ (ns)
$S_{as-grown}$	615.8	479.2	148.6	0.6	2.7	10.3	6.1
S_{350}	1160.3	365.7	17.1	1.1	5.5	35.0	8.5
S_{450}	1078.4	406.0	71.4	1.0	4.1	33.9	17.7

Fig. 5 (a) UV-spectra of the mixed phase before and after heating at 200 °C (b) the distribution of resistance value before and after illumination of under IR radiation.

due to oxygen vacancies, and the peaks at shorter wavelengths in UV are due to the transitions from higher V_{3d} states to O_{2p} bands.[37] Apparently, the more peaks in NIR are observed in amorphous and mixed phase samples due to large number of defects and oxygen vacancies compared to V_2O_5. The increased bandgap of mixed phase can be caused by the Burstein–Moss shift in PL spectra as a result of degenerate semiconducting behaviour of V_7O_{16}.[23,47]

To further investigate the nature of defects, we have measured the carrier life using TRPL as shown in Fig. 4(b) of $S_{as-grown}$, S_{350}, and S_{450}. In TRPL, the peak intensity decay (I_{TRPL}) with time (t) can be fitted using the following equation

$$I_{TRPL}(t) = \sum_{i}^{n} A_i e^{-t/\tau_i}$$

where A_i, τ_i are constants representing the amplitude and the lifetime of carriers. Here, we have used component $i = 3$ to fit the experimental curve and calculated the average decay time using the following expression

$$\tau_{av} = \frac{A_1\tau_1^2 + A_2\tau_2^2 + A_3\tau_3^2}{A_1\tau_1 + A_2\tau_2 + A_3\tau_3}$$

The extracted fitting parameters and average decay time are shown in Table 2. The decay constants τ_1 and τ_2 attributes to the fast decay through trap-mediated recombination, while τ_3 corresponds to slow decay through radiative recombination.[37] The average decay time of S_{450} is higher compared than other two samples due to the reduction in oxygen vacancies in the samples, which agrees well with the previous observations.[48] These results are in good agreement with the Urbach energy measurements shown in Fig. 3(b).

Finally, we demonstrate the sensitivity of our mixed phase sample by heating and IR radiation as shown in Fig. 5(a) and (b) respectively. Fig. 5(a) illustrate the optical transmission taken before and after heating the sample at 200 °C outside and then transferred to the UV-vis spectroscopy. Interestingly, a clear change in the transmission was only observed for the wavelengths higher than ~600 nm in near-IR (NIR) region. Indeed, no major change in the spectrum was observed in the visible range, indicating that these films are more sensitive to IR. Clearly, there will be some variations in temperature while taking the optical measurements, but the overall spectrum is always fully recovered as the samples is cooled back to the room temperature naturally.

Also, V_7O_{16} being a degenerate semiconductor could also be suitable candidate for NIR plasmonics. Indeed, the broad peak ~650 nm in the UV-vis spectrum could be due to the NIR plasmons absorption.[23] Since the plasmonic frequency $\omega_p = \sqrt{ne^2/\varepsilon_0 m^*}$ is related to the carrier concentration (n) and the effective mass (m^*), where e and ε_0 are electronic charge and the permittivity of free space, respectively. The measured value of resonant frequency ~4.6×10^{14} Hz gives the carrier concentration ~10^{20} to 10^{21} cm^{-3}, which is also consistent with our conductivity values considering the theoretical values of mobilities and effective mass of vanadium oxides ($1-1.7m_e$).[49,50] The IR sensitivity in optical transmission is due to the plasmonic absorption and consistent with the earlier studied on the mixed phase of metallic VO_2 and insulating V_2O_5.[33] Also, the increase in resistance under IR radiation seen in Fig. 5(b) could be due to the electron–electron and electron–phonon scatterings as observed in metals and degenerate semiconductors in the resistance *versus* temperature measurements. Clearly, more low temperature transport measurements are required to further investigate the transport properties, but these results are encouraging for their promising use in smart-windows and IR sensors.

Conclusions

In conclusion, we provide a detailed in-depth understanding of electronic and optical properties of V_7O_{16} and systematically tune the electronic and optical properties of a mixed phase by changing the V^{4+} and V^{5+} contents. We report a strong modulation in the conductivity and optical transmission with infrared radiation and temperature. These results are very

promising for vanadium oxide based uncooled-IR sensors and smart windows that can be grown at low temperatures using a commercially viable cathodic vacuum arc-deposition technique.

Conflicts of interest

There are no conflicts to declare.

Acknowledgements

References

1 A. Rogalski, *Infrared Phys. Technol.*, 2002, **43**, 187–210.

2 J. Wang, H. Fang, X. Wang, X. Chen, W. Lu and W. Hu, *Small*, 2017, **13**, 1–17.

3 A. Rogalski, *J. Appl. Phys.*, 2003, **93**, 4355–4391.

4 M. Strojnik, M. D'Acunto and A. Rogalski, *Appl. Opt.*, 2016, **55**, ITA1.

5 D. Benyahia, Ł. Kubiszyn, K. Michalczewski, A. Kębłowski, P. Martyniuk, J. Piotrowski and A. Rogalski, *Opt. Quantum Electron.*, 2016, **48**, 1–7.

6 K. Nakade, T. Kashiwagi, Y. Saiwai, H. Minami, T. Yamamoto, R. A. Klemm and K. Kadowaki, *Sci. Rep.*, 2016, **6**, 23178.

7 A. J. Kreisler and A. Gaugue, *Supercond. Sci. Technol.*, 2000, **13**, 1235.

8 F. J. Morin, *Phys. Rev. Lett.*, 1959, **3**, 34–36.

9 M. Imada, A. Fujimori and Y. Tokura, *Rev. Mod. Phys.*, 1998, **70**, 1039–1263.

10 C. Chen, X. Yi, J. Zhang and B. Xiong, *Int. J. Infrared Millimeter Waves*, 2001, **22**, 53–58.

11 Q. Cheng, T. Bui, M. Almasri and S. Paradis, *IEEE Sens. J.*, 2011, **11**, 167–175.

12 M. Nishikawa, T. Nakajima, T. Manabe, T. Okutani and T. Tsuchiya, *Mater. Lett.*, 2010, **64**, 1921–1924.

13 J. Jeong, N. Aetukuri, T. Graf, T. D. Schladt, M. G. Samant and S. S. P. Parkin, *Science*, 2013, **339**, 1402–1405.

14 P. Shvets, O. Dikaya, K. Maksimova and A. Goikhman, *J. Raman Spectrosc.*, 2019, **50**, 1226–1244.

15 M. Yuan, T. Huang, S. Wang, R. Zhang, Y. Yang, W. Yang, W. Wei, T. Zhang, W. Dong, X. Chen and N. Dai, *ACS Appl. Electron. Mater.*, 2019, **1**, 2308–2313.

16 J. Huotari, J. Lappalainen, J. Eriksson, R. Bjorklund, E. Heinonen, I. Miinalainen, J. Puustinen and A. Lloyd Spetz, *J. Alloys Compd.*, 2016, **675**, 433–440.

17 M. Roppolo, C. B. Jacobs, S. Upreti, N. A. Chernova and M. S. Whittingham, *J. Mater. Sci.*, 2008, **43**, 4742–4748.

18 R. T. Rajendra Kumar, B. Karunagaran, D. Mangalaraj, S. K. Narayandass, P. Manoravi, M. Joseph and V. Gopal, *Sens. Actuators, A*, 2003, **107**, 62–67.

19 M. M. Qazilbash, M. Brehm, B. G. Chae, P. C. Ho, G. O. Andreev, B. J. Kim, S. J. Yun, A. V. Balatsky, M. B. Maple, F. Keilmann, H. T. Kim and D. N. Basov, *Science*, 2007, **318**, 1750–1753.

20 V. R. Morrison, R. P. Chatelain, K. L. Tiwari, A. Hendaoui, A. Bruhacs, M. Chaker and B. J. Siwick, *Science*, 2014, **346**, 445–448.

21 P. T. P. Le, K. Hofhuis, A. Rana, M. Huijben, H. Hilgenkamp, G. A. J. H. M. Rijnders, J. E. ten Elshof, G. Koster, N. Gauquelin, G. Lumbeeck, C. Schüßler-Langeheine, H. Popescu, F. Fortuna, S. Smit, X. H. Verbeek, G. Araizi-Kanoutas, S. Mishra, I. Vaskivskyi, H. A. Dürr and M. S. Golden, *Adv. Funct. Mater.*, 2020, **30**, 1900028.

22 A. Rana, C. Li, G. Koster and H. Hilgenkamp, *Sci. Rep.*, 2020, **10**, 2–7.

23 Q. Wang, M. Brier, S. Joshi, A. Puntambekar and V. Chakrapani, *Phys. Rev. B*, 2016, **94**, 1–12.

24 S. Tepavcevic, H. Xiong, V. R. Stamenkovic, X. Zuo, M. Balasubramanian, V. B. Prakapenka, C. S. Johnson and T. Rajh, *ACS Nano*, 2012, **6**, 530–538.

25 Y. Wang, K. Takahashi, K. Lee and G. Cao, *Adv. Funct. Mater.*, 2006, **16**, 1133–1144.

26 R. Baddour-Hadjean, M. Safrany Renard, N. Emery, L. T. N. Huynh, M. L. P. Le and J. P. Pereira-Ramos, *Electrochim. Acta*, 2018, **270**, 129–137.

27 K. Schneider and W. Maziarz, *Sensors*, 2018, **2**, 2–6.

28 M. Yu, X. Liu, Y. Wang, Y. Zheng, J. Zhang, M. Li, W. Lan and Q. Su, *Appl. Surf. Sci.*, 2012, **258**, 9554–9558.

29 J. Huotari, J. Lappalainen, J. Puustinen and A. Lloyd Spetz, *Sens. Actuators, B*, 2013, **187**, 386–394.

30 T. K. Le, P. V. Pham, C. L. Dong, N. Bahlawane, D. Vernardou, I. Mjejri, A. Rougier and S. W. Kim, *J. Mater. Chem. C*, 2022, **10**, 4019–4071.

31 C. M. Lampert, *Mater. Today*, 2004, **7**, 28–35.

32 S. Kumar, A. Qadir, F. Maury and N. Bahlawane, *ACS Appl. Mater. Interfaces*, 2017, **9**, 21447–21456.

33 S. Y. Li, G. A. Niklasson and C. G. Granqvist, *Thin Solid Films*, 2012, **520**, 3823–3828.

34 J. Huotari, R. Bjorklund, J. Lappalainen and A. L. Spetz, *Procedia Eng.*, 2014, **87**, 1035–1038.

35 C. K. Christensen, E. D. Bøjesen, D. R. Sørensen, J. H. Kristensen, J. K. Mathiesen, B. B. Iversen and D. B. Ravnsbæk, *ACS Appl. Nano Mater.*, 2018, **1**, 5071–5082.

36 Z. Yang, C. Ko and S. Ramanathan, *Annu. Rev. Mater. Res.*, 2011, **41**, 337–367.

37 T. K. Le, M. Kang, S. W. Han and S. W. Kim, *RSC Adv.*, 2018, **8**, 41317–41322.

38 G. Silversmit, D. Depla, H. Poelman, G. B. Marin and R. De Gryse, *J. Electron Spectrosc. Relat. Phenom.*, 2004, **135**, 167–175.

39 A. Rana, A. Patra, M. Annamalai, A. Srivastava, S. Ghosh, K. Stoerzinger, Y.-L. Lee, S. Prakash, R. Y. Jueyuan, P. S. Goohpattader, N. Satyanarayana, K. Gopinadhan, M. M. Dykas, K. Poddar, S. Saha, T. Sarkar, B. Kumar,

C. S. Bhatia, L. Giordano, Y. Shao-Horn and T. Venkatesan, *Nanoscale*, 2016, **8**, 15597–15603.

40 J. Mendialdua, R. Casanova and Y. Barbaux, *J. Electron Spectrosc. Relat. Phenom.*, 1995, **71**, 249–261.

41 G. Silversmit, D. Depla, H. Poelman, G. B. Marin and R. De Gryse, *Surf. Sci.*, 2006, **600**, 3512–3517.

42 R. Baddour-Hadjean, M. B. Smirnov, V. Y. Kazimirov, K. S. Smirnov and J. P. Pereira-Ramos, *J. Raman Spectrosc.*, 2015, **46**, 406–412.

43 A. G. S. Filho, O. P. Ferreira, E. J. G. Santos, J. M. Filho and O. L. Alves, *Nano Lett.*, 2004, **4**, 2099–2104.

44 R. Baddour-Hadjean, M. B. Smirnov, K. S. Smirnov, V. Y. Kazimirov, J. M. Gallardo-Amores, U. Amador, M. E. Arroyo-de Dompablo and J. P. Pereira-Ramos, *Inorg. Chem.*, 2012, **51**, 3194–3201.

45 T. Blanquart, J. Niinistö, M. Gavagnin, V. Longo, M. Heikkilä, E. Puukilainen, V. R. Pallem, C. Dussarrat, M. Ritala and M. Leskelä, *RSC Adv.*, 2013, **3**, 1179–1185.

46 M. Kang, S. W. Kim, Y. Hwang, Y. Um and J. W. Ryu, *AIP Adv.*, 2013, **3**, 052129.

47 T. S. Moss, *Proc. Phys. Soc. B*, 1954, **67**, 775.

48 U. Özgür, A. Teke, C. Liu, S. J. Cho, H. Morkoç and H. O. Everitt, *Appl. Phys. Lett.*, 2004, **84**, 3223–3225.

49 A. S. Barker, H. W. Verleur and H. J. Guggenheim, *Phys. Rev. Lett.*, 1966, **17**, 1286–1289.

50 M. M. Qazilbash, M. Brehm, B.-G. Chae, P.-C. Ho, G. O. Andreev, B.-J. Kim, S. J. Yun, A. V. Balatsky, M. B. Maple, F. Keilmann, H.-T. Kim and D. N. Basov, *Science*, 2007, **318**, 1750–1753.